Tension-dependent stabilization of E-cadherin limits cell–cell contact expansion in zebrafish germ-layer progenitor cells

Jana Slováková[a,b,1], Mateusz Sikora[a,c,d,1], Feyza Nur Arslan[a], Silvia Caballero-Mancebo[a], S. F. Gabriel Krens[a], Walter A. Kaufmann[a], Jack Merrin[a], and Carl-Philipp Heisenberg[a,2]

[a]Institute of Science and Technology Austria, A-3400 Klosterneuburg, Austria; [b]Department of Theoretical Biophysics, Institute of Molecular Biotechnology, Vienna, 1030 Austria; [c]Max Planck Institute of Biophysics, D-60438 Frankfurt am Main, Germany; and [d]Faculty of Physics, University of Vienna, 1090 Vienna, Austria

Edited by Alpha Yap, Institute for Molecular Bioscience, University of Queensland, Brisbane, QLD, Australia; received December 13, 2021; accepted December 29, 2021 by Editorial Board Member Yale E. Goldman

Tension of the actomyosin cell cortex plays a key role in determining cell–cell contact growth and size. The level of cortical tension outside of the cell–cell contact, when pulling at the contact edge, scales with the total size to which a cell–cell contact can grow [J.-L. Maître *et al.*, *Science* 338, 253–256 (2012)]. Here, we show in zebrafish primary germ-layer progenitor cells that this monotonic relationship only applies to a narrow range of cortical tension increase and that above a critical threshold, contact size inversely scales with cortical tension. This switch from cortical tension increasing to decreasing progenitor cell–cell contact size is caused by cortical tension promoting E-cadherin anchoring to the actomyosin cytoskeleton, thereby increasing clustering and stability of E-cadherin at the contact. After tension-mediated E-cadherin stabilization at the contact exceeds a critical threshold level, the rate by which the contact expands in response to pulling forces from the cortex sharply drops, leading to smaller contacts at physiologically relevant timescales of contact formation. Thus, the activity of cortical tension in expanding cell–cell contact size is limited by tension-stabilizing E-cadherin–actin complexes at the contact.

cell adhesion | cell–cell contact formation | mechanosensing

For multicellular organisms to form, cells need to establish stable and long-lasting contacts. Consequently, insight into the molecular and cellular mechanisms by which cell–cell contacts are being formed and maintained is central for understanding how multicellularity has emerged in evolution. Adhesion between cells is mediated by various cell–cell adhesion molecules, among which cadherins constitute a key family of adhesion receptors mediating selective Ca^{2+}-dependent cell–cell adhesion (1, 2). While much progress has been made in identifying how cadherin adhesion molecules can trigger cell–cell contact formation by binding to each other and associated molecules, such as catenins (3–5), comparably little is known on how cadherins transduce forces between cells and how such force transduction feeds back on the organization and function of cadherins at cell–cell contacts.

Cadherins—and in particular, classical cadherins—are thought to function in cell–cell contact formation in three different ways (6, 7). 1) They promote cell–cell contact formation by directly lowering interfacial tension at the cell–cell contact zone (8). How cadherins achieve this is not yet entirely clear, but the generation of lateral pressure through cadherin-mediated molecular crowding at the contact zone has been proposed as one potential effector mechanism (9, 10). 2) Signaling from cadherins modulates the actomyosin cytoskeleton at the contact site, thereby controlling contact growth and maintenance (11). Effector molecules involved in this process include RhoA and Arp2/3, which both are repressed when cadherins bind over the contact, and Rac, which is activated upon cadherin binding (12, 13). 3) Cadherins transduce pulling forces from the contractile actomyosin cortices of the contacting cells over the contact site (6, 14, 15). This force transduction allows the contact to grow and reach steady state after those forces are balanced at the contact. Data on cultured cells and primary cells from zebrafish embryos support a critical function of cadherins in contact expansion. They are thought to disassemble the actomyosin cortex at the contact site and mechanically couple the cortices of the contacting cells at the contact edge (6, 16). These observations led to a model where pulling forces at the contact edge, originating from the contractile cortices of the contacting cells, are transduced by cadherins over the contact and drive contact expansion. Consequently, the size of the contact is expected to scale with the ratio of cortical tension at the cell–cell vs. the cell–medium interface (6, 9).

Cadherins at cell–cell contacts not only transduce forces between the contacting cells but are also affected by the forces to which they are subjected. Studies on culture cells have provided evidence that tension at cadherin cell–cell adhesion sites promotes cadherin clustering and reduces their turnover at the contact site (16–18). How tension functions in those processes

Significance

Cell–cell contact formation is a key step in the evolution of multicellularity. While the molecular and cellular processes underlying cell–cell adhesion and contact formation have been extensively studied, comparably little is known about the physical principles guiding these processes. Actomyosin cortex tension differentially applied at the cell–cell and cell–medium interfaces was shown to promote expansion of the cell–cell contacts. Here, we uncover a nonlinear relationship between cortex tension and cell–cell contact size; in a low-tension regime, cell–cell contact size positively scales with cortex tension, while the high-tension regime promotes small contacts. This change in behavior is due to tension decreasing the turnover of adhesion molecules at the cell–cell contact, limiting contact expansion.

Author contributions: J.S., M.S., and C.-P.H. designed research; J.S. and M.S. performed research; F.N.A., S.C.-M., W.A.K., and J.M. contributed new reagents/analytic tools; J.S. and M.S. analyzed data; and J.S., M.S., S.F.G.K., and C.-P.H. wrote the paper.

The authors declare no competing interest.

This article is a PNAS Direct Submission. A.Y. is a guest editor invited by the Editorial Board.

[1]J.S. and M.S. contributed equally to this work.

[2]To whom correspondence may be addressed. Email: heisenberg@ist.ac.at.

This article contains supporting information online at http://www.pnas.org/lookup/suppl/doi:10.1073/pnas.2122030119/-/DCSupplemental.

Published February 14, 2022.

is not yet fully understood, but tension-induced stabilization of filamentous actin (F-actin) (16, 19, 20) and unfolding of α-catenin (21), a key component of the cadherin adhesion complex (22, 23), are involved. Unfolding of α-catenin is thought to reveal cryptic binding sites to Vinculin (21, 24), which again enhances binding of α-catenin to F-actin by simultaneously binding to both molecules (17, 20, 25, 26).

Yet, how mechanosensing of cadherin cell–cell adhesion sites affects the function of cadherins in contact expansion and maintenance remains unclear. To address this question, we tested how changes in cortex tension affect contact expansion of zebrafish primary germ-layer progenitor cells. Contrary to previous expectations (6), we found that above a critical threshold level of tension, the size of cell–cell contacts becomes smaller rather than bigger. We further found that this restricting influence of cortex tension on contact growth is due to high tension promoting cytoskeletal anchoring of E-cadherin, leading to enhanced clustering and stability of E-cadherin at the contact.

Results

To test whether the ratio of cortical tensions at the cell–medium to cell–cell interface directly scales with cell–cell contact size, as previously suggested (6, 9), we sought to analyze the effect of a wide range of cortical tension ratios on contact formation. In order to examine cell–cell contact formation in primary vertebrate cells, we turned to zebrafish germ-layer progenitor cells, previously used to study the role of cortical tension in contact expansion (6). Specifically, we imaged ectoderm progenitor cell doublets either mounted in polymeric wells, allowing us to monitor cell–cell contact organization at high resolution (Fig. 1*A*), or placed on nonadhesive substrates for high-throughput analysis of contact expansion. Consistent with previous observations (6), we found that reducing cortical tension at the cell–medium interface (named "cortical tension" for the remainder of the manuscript) in cell doublets by exposing them to 10 μM myosin II inhibitor blebbistatin (Bb) and thus, decreasing the ratio of cortical tensions at the cell–medium to cell–cell interface—assuming that cortical tension at the cell–cell interface is uniformly down-regulated independently of the total level of cortical tension in the adhering cells (6, 9)—severely reduced expansion of the cell–cell contact surface area (A_c) (Fig. 1 *B* and *C* and *SI Appendix*, Fig. S1). Contrary to the model predictions, however, when performing the reverse experiment and strongly increasing cortical tension by exposing cell doublets to 50 nM lysophosphatidic acid (LPA) (27) or overexpressing constitutively active (ca) RhoA in the contacting cells (28) and thus, increasing the ratio of cortical tensions at the cell–medium to cell–cell interface (*SI Appendix*, Fig. S2) (6, 9), both the initial rate of contact expansion (0 to 3 min after contact initiation) and the size of A_c after 15 min of contact formation were reduced rather than increased (Fig. 1 *B* and *C* and *SI Appendix*, Fig. S1). Notably, the effect of LPA on contact expansion became already apparent during the first minute of contact formation (Fig. 1*C* and *SI Appendix*, Fig. S1), suggesting that high cortical tension restricts contact expansion within seconds after contact initiation. Together, these findings contrast previous observations that the ratio of cortical tensions at the cell–medium to cell–cell interface directly scales with cell–cell contact size (6, 9).

To systematically investigate how changes in cortical tension affect contact expansion in doublets, we determined to what extent cortical tension is altered in progenitor cells upon exposure to Bb or different concentrations of LPA by employing atomic force microscopy (AFM) (29, 30), and how those changes relate to contact expansion. We found that A_c was maximized when cortical tension was left unaltered, while it dropped when cortical tension was either elevated in the presence of LPA (5 to 50 nM) or diminished upon exposure to Bb (10 μM) (Fig. 1*D*). This suggests that the threshold level of cortical tension delineating the transition point from where on cortical tension is not promoting but inhibiting contact expansion is close to the cortical tension level of untreated progenitor cells. To exclude the possibility that the effect of LPA on cell–cell contact expansion is not due to its activity in elevating cortical contractility but rather, by modulating other potential target processes, such as actin polymerization (31), we first tested whether general cell properties, such as their overall size and distribution of plasma membrane in contacting vs. noncontacting regions, are affected in LPA-treated doublets. None of these features showed consistent changes upon LPA treatment (*SI Appendix*, Fig. S3), arguing against LPA affecting general cell properties that might secondarily impact contact formation. To more specifically address whether LPA affects contact formation by up-regulating cortex tension, we reduced myosin II activity in LPA-treated progenitor cell doublets and determined how this affects the ability of LPA in restricting contact expansion. While cell–cell contact expansion was strongly restricted in cell doublets exposed to 50 nM LPA, this restriction was abrogated when 10 μM Bb was also added to the culture medium (Fig. 1*E*). This confirms that LPA restricts cell–cell contact expansion by elevating cortical actomyosin contractility.

Collectively, our findings so far suggest that cortical tension—contrary to the expectations of the prevalent model where the size of the contact is expected to directly scale with the level of cortex tension and thus, the ratio of cortical tension at the cell–medium to cell–cell interface (6, 9)—has a dual function in controlling contact expansion, with low to normal levels of cortical tension promoting and high levels of cortical tension inhibiting contact expansion.

To explore the mechanisms by which high cortical tension limits contact expansion, we turned to previous observations that cortical tension might increase cadherin adhesion complex clustering and stability at cell–cell contact sites (16, 32). To visualize cadherin complex dynamics in progenitor cell doublets, we took advantage of a transgenic line [Transgene(Tg)*(ctnna-citrine)ct3a*], which expresses a Citrine-tagged version of α–E-catenin (Ctnna1) under its endogenous promoter that colocalizes with E-cadherin/Cdh1 (*SI Appendix*, Fig. S4), the prime classical cadherin mediating zebrafish germ-layer progenitor cell–cell contact formation (29). Analyzing the subcellular distribution of Ctnna1 at the cell–cell contact in control and LPA-treated doublets (50 nM) revealed a stronger accumulation of Ctnna1 at the contact edge in treated compared to control doublets (Fig. 2*A*). This enhanced accumulation of Ctnna1 at the contact edge was accompanied by similar changes in cortical actin localization (Fig. 2*A*). Myosin II, in contrast, did not show any detectable accumulation at the contact edge in both treated and control doublets (Fig. 2*A*). High-resolution analysis of Ctnna1 distribution at the contact further showed both brighter and larger Ctnna1 clusters in LPA-treated vs. control doublets (Fig. 2*B*), which colocalized with E-cadherin/Cdh1 (*SI Appendix*, Fig. S4). Together, this suggests that elevating cortical tension promotes E-cadherin/Ctnna1 adhesion complex accumulation and clustering at the contact edge.

To analyze how cortical tension affects Ctnna1 adhesion clusters and their association to the actin cytoskeleton at high resolution, we performed correlative light and electron microscopy (CLEM) on E-cadherin clusters in control and LPA-treated doublets (Fig. 2*C*). By labeling F-actin with Phalloidin, we were able to determine how putative E-cadherin adhesion complexes were associated with the actin cytoskeleton. Consistent with our high-resolution light microscopy analysis (Fig. 2*B*), we found junctional structures closely resembling adherens junctions at the contact of both control and LPA-treated doublets (Fig. 2 *C* and *D*). Moreover, we observed actin accumulations adjacent to those structures, which appeared enlarged in LPA-treated

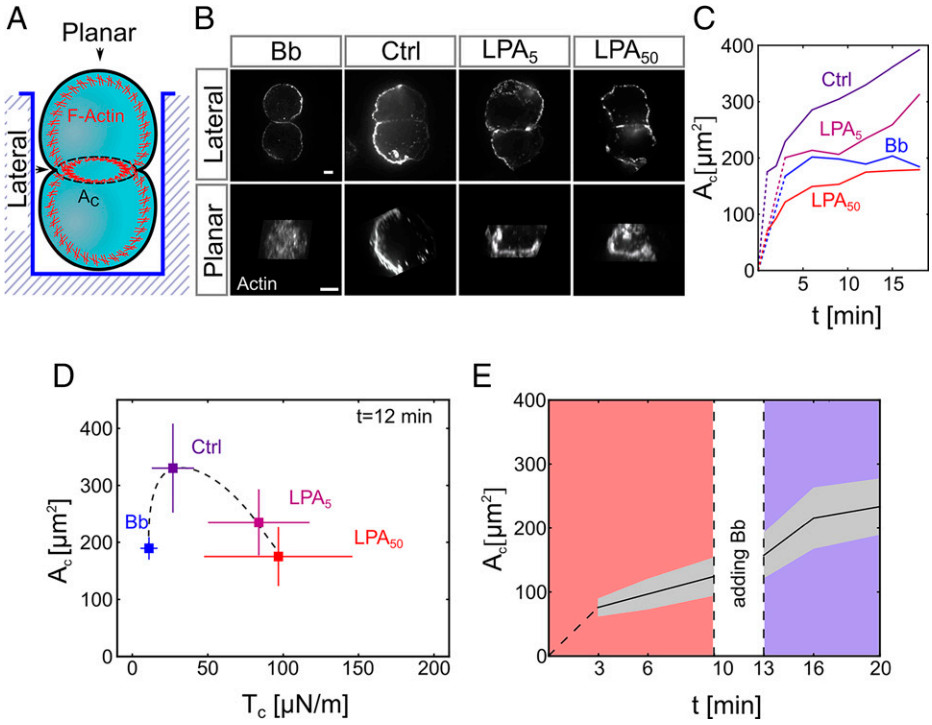

Fig. 1. Cortical tension limits contact expansion in cell doublets. (*A*) Schematic of the experimental setup for live imaging of progenitor cell doublets. Doublets were placed in polymeric wells for maintaining their contact within the focal plane while being imaged from the bottom. (*B*) Planar and lateral views of the actin cell cortex in progenitor cell doublets (10-min contact time) visualized by Phalloidin (F-actin) in control (Ctrl) doublets and doublets exposed to Bb (10 μM) or LPA (5 and 50 nM). (Scale bar: 5 μm.) (*C*) Cell–cell contact size (A_c) as a function of contact time in control doublets, doublets exposed to Bb (10 μM), or different concentrations of LPA (1 to 50 nM). Dotted lines connect contact formation (0 min) with the first time point when data were collected. Error bars (SD) are shown in *SI Appendix*, Fig. S1. Ctrl: $N = 9$, $n =$ (1 min: 30, 2 min: 26, 3 min: 30, 6 min: 24, 9 min: 24, 12 min: 24, 15 min: 22, 18 min: 22); LPA_5: $N = 1$, $n = 10$ (for each time point); Bb: $n = 1$, $n =$ (3 for each time point); LPA_{50}: $N = 7$, $n =$ (1 min: 32, 2 min: 32, 3 min: 33, 6 min: 21, 9 min: 21, 12 min: 21, 15 min: 21, 18 min: 20). (*D*) Cell–cell contact size (A_c) at 12-min contact time for control doublets and doublets exposed to Bb (10 μM) or different amounts of LPA (5 to 50 nM) plotted against cortical tension (T_c) values measured by AFM. Error bars denote SD. For T_c measurements, $N = 3$, (single-cell Ctrl) $n = 287$, (single-cell Bb) $n = 88$, (single-cell LPA_5) $n = 142$, and (single-cell LPA_{50}) $n = 294$. For A_c measurements, N and n are the same as in *C* (time point 12 min). (*E*) A_c in doublets exposed to 50 nM LPA as a function of time in culture before and after adding 10 μM Bb to the culture medium. The gray area denotes SD ($N = 3$; $n = 16$). If not stated otherwise, N corresponds to the number of experiments, and n corresponds to the number of cell doublets.

doublets (Fig. 2*D*), suggesting that cortical tension might increase the size not only of E-cadherin clusters but also, of the adjacent actin accumulations. To further test this notion, we performed high-resolution fluorescence microscopy of contacts stained for both Ctnna1 and F-actin in control and LPA-treated doublets, revealing larger actin accumulations adjacent to larger Ctnna1 clusters in LPA-treated compared with control doublets (Fig. 2*E*).

Tension-induced cadherin cluster formation at cell–cell contacts has previously been associated with reduced adhesion molecule turnover (16). To test whether adhesion complex turnover at germ-layer progenitor cell–cell contacts is affected by changes in cortical tension, we performed fluorescence recovery after photobleaching (FRAP) experiments of Ctnna1 in control and LPA-treated doublets (Fig. 3*A*). Interestingly, by using kymographs to outline spatiotemporal changes in Ctnna1 intensity after photobleaching (Fig. 3*B*) and quantifying those changes as a function of time (Fig. 3*C*), we found that within seconds—the timescale relevant for LPA affecting contact expansion in progenitor cell doublets (Fig. 1*C*)—recovery of Ctnna1 from adjacent nonbleached areas of the contact edge was strongly slowed down in progenitor cell doublets exposed to 50 nM LPA (Fig. 3*C*). This suggests that increasing cortical tension not only increases cadherin clustering but also, reduces cadherin adhesion complex turnover at the contact site.

Next, we asked how cortical tension promotes E-cadherin clustering and stability. Previous studies have suggested that cortical actomyosin tension transduced to the cadherin adhesion complex promotes anchoring of the complex to the cortex and that increased cortical anchoring enhances cadherin stability and clustering (16, 33, 34). For testing whether such a mechanism can also explain the observed effect of cortical tension on E-cadherin clustering and turnover in germ-layer progenitor cell doublets, we first determined how tension within the E-cadherin adhesion complex is changed upon alterations in cortical actomyosin tension. For visualizing tension within the E-cadherin adhesion complex, we took advantage of previous observations that tension at cadherin adhesion sites leads to unfolding of α-catenin and as a result of this, enhanced recruitment of Vinculin to those sites (5, 20, 35, 36). Determining the amount of Vinculin at the contact edge in control vs. LPA-treated progenitor cell doublets revealed strong recruitment of Vinculin, colocalizing with α-catenin (Ctnna1) at the contact edge, upon exposure to LPA (50 nM) already 1 min after contact initiation, while no Vinculin was detectable in untreated control doublets (*SI Appendix*, Fig. S5). This suggests that LPA increases tension within the cadherin adhesion complex.

To investigate how increased cortical tension and thus, tension within the cadherin adhesion complex affects anchoring of the adhesion complex to the actomyosin cortex, we used a dual-micropipette aspiration assay (DPA) to determine the deadhesion strength of control and LPA-treated progenitor cell doublets (6). We have previously shown that when separating progenitor cell doublets using DPA, the E-cadherin adhesion complex at the

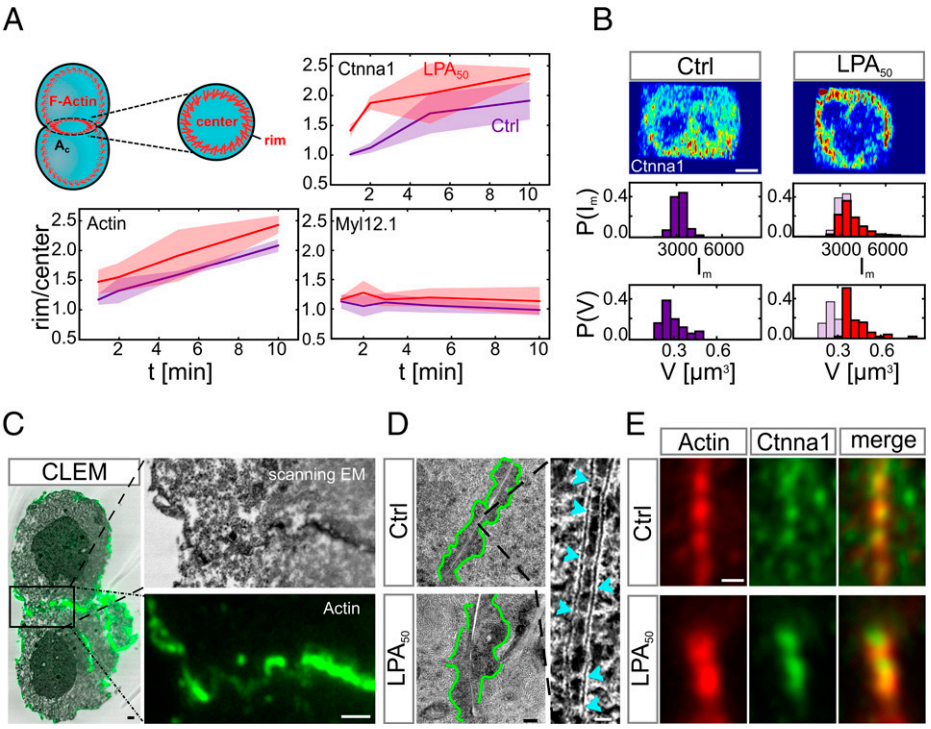

Fig. 2. Cortical tension triggers Ctnna1/F-actin clustering at the contact of cell doublets. (*A*) Rim to center intensity ratios of core components of the cadherin adhesion complex in doublets. The schematic in *Left* shows the rim and center regions of the cell–cell contact where the fluorescence mean intensities were measured in control doublets (red line) and doublets exposed to LPA 50 nM (blue line). Doublets were fixed and analyzed for each time point separately (1-, 2-, 5-, and 10-min contact time). F-actin was visualized by Phalloidin with $n = 3$; (Ctrl) $n = 5$, 3, 3, and 3 (corresponding to the different contact times mentioned above); and (LPA) $n = 6$, 5, 4, and 5. Ctnna1 was visualized by immunohistochemistry with $n = 3$; (Ctrl) $n = 5$, 3, 5, and 5; and (LPA) $n = 4$, 3, 4, and 3. Myosin II was visualized by Myl12.1-eGFP expression with $n = 1$; (Ctrl) $n = 9$, 8, 7, and 8; and (LPA) $n = 5$, 5, 4, and 2. Shadowed areas denote SD. (*B*) Exemplary subdiffraction limited confocal images of Ctnna1 subcellular distribution at the cell–cell contact of control doublets (*Left*) and doublets exposed to 50 nM LPA (*Right*). Quantifications below show cluster mean intensity (I_m) and volumes (V) of the 50 largest clusters of each cell–cell contact. Blue shadows in *Right* denote control conditions. (Ctrl) $N = 1$ and $n = 3$; (LPA) $N = 1$ and $n = 5$. (Scale bar: 5 µm.) (*C*) CLEM images with F-actin visualized by phalloidin–Alexa-488 (green). *Right* shows zoomed-in images of the boxed region in *Left*. (Scale bars: 1 µm.) (*D*, *Left*) Electron microscopy (EM) images of electron-dense clusters (outlined with green) at cell–cell contacts in control doublets (*Upper*) and doublets exposed to 50 nM LPA (*Lower*). (Scale bar: 200 nm.) *D*, *Right* is a zoomed-in image of cadherin-like clusters with individual clusters depicted by light blue arrowheads. (Scale bar: 20 nm.) (*E*) Representative Airy Scan images of F-actin (red) and Ctnna1 (green) colocalizing in clusters at the cell–cell contact of control doublets (*Upper*) and doublets exposed to 50 nM LPA (*Lower*). Cell doublets were fixed after 30-min contact time and visualized by Phalloidin (F-actin) and immunohistochemistry (Ctnna1). If not stated otherwise, *N* corresponds to the number of experiments, and *n* corresponds to the number of cell doublets. (Scale bar: 2 µm.)

cell–cell contact ruptures first at its linkage to the actomyosin cortex, suggesting that the deadhesion strength is limited by the cortical anchoring strength of the E-cadherin adhesion complex and thus, can be used to determine cytoskeletal anchoring of E-cadherin in those cells (6). Comparing the deadhesion strength of progenitor cell doublets in the presence or absence of LPA revealed higher contact stress (deadhesion force divided by the contact size to normalize for variations in contact size) when cell cortex tension was elevated in cell doublets by exposing them to 50 nM LPA (Fig. 4*A*; deadhesion forces are shown in *SI Appendix*, Fig. S6*A*). Given that the total amount of clustered and unclustered E-cadherin at the contact was not increased upon LPA treatment (as measured by determining the integrated intensity of Ctnna–citrine at the cell–cell contact with Ctrl = 7.5 ± 2.8 a.u. [$N = 3$, $n = 2$, 6, 6] and LPA = 4.8 ± 1.6 a.u. [$N = 3$, $n =$ 1, 6, 2]) (Fig. 2 *A* and *B*), this suggests that cortical tension promotes anchoring of E-cadherin to the actomyosin cortex in progenitor cell doublets.

To determine whether increased cortical anchoring of the cadherin adhesion complex by tension enhances cadherin clustering at cell–cell contacts, we analyzed how changes in cortical anchoring affect E-cadherin clustering in progenitor cell doublets. For modulating the anchoring strength of the E-cadherin to the actomyosin cortex in these cells, we sought to interfere with F-actin network stability and consequently, the ability of the cadherin complex to establish stable contact with the actomyosin cortex rather than changing specific cadherin adhesion complex components, whose anchoring function is not yet fully understood (37, 38). To modulate cortical actin network stability, we exposed doublets to Latrunculin (Latr), blocking actin polymerization and thus, destabilizing the cortical actin network, or Jasplakinolide (Jasp), promoting actin polymerization and network stability (16, 34). First, we analyzed how exposure to Latr and Jasp affects cortical anchoring of the E-cadherin complex by determining the deadhesion force of progenitor cell doublets as a readout of the cortical anchoring strength in the presence of Latr or Jasp. The deadhesion force of cell doublets was decreased when F-actin was destabilized in the presence of 300 nM Latr (Fig. 4*B*), suggesting that exposure to Latr reduces the cortical anchoring strength of the E-cadherin adhesion complex. Conversely, when progenitor cell doublets were exposed to 100 nM Jasp to stabilize the F-actin network, the apparent deadhesion force remained largely unchanged (Fig. 4*B*). However, multiple actin-containing tethers were typically observed between the separating cells (Fig. 4*B*), suggesting that contacts were not fully separated, which also prevented us from reliably determining contact stress under those conditions (*SI Appendix*, Fig. S6*B*). While these measurements did not reveal the complete separation force of Jasp-treated doublets, they show that the cortical anchoring strength of E-cadherin in the

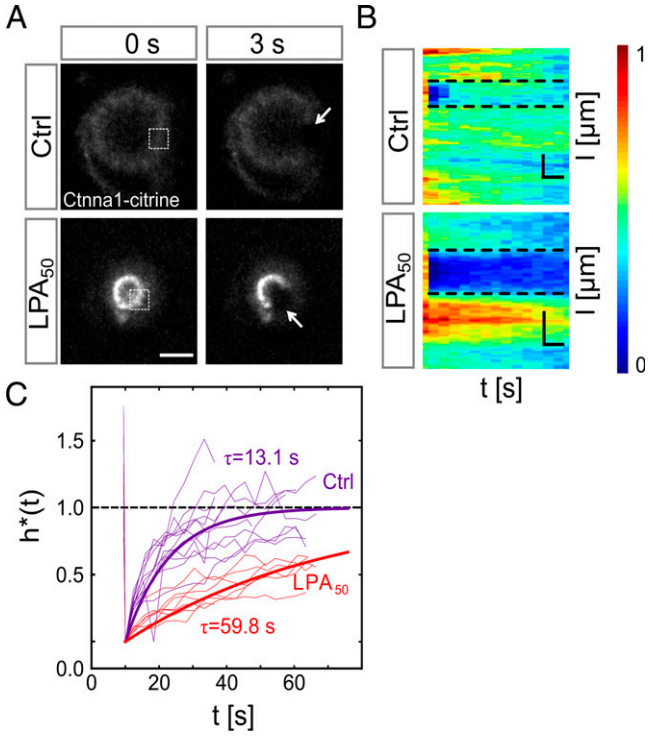

Fig. 3. Cortical tension reduces Ctnna1 turnover at the contact of cell doublets. (*A*) FRAP analysis of Ctnna1 turnover at the contact of progenitor cell doublets. Fluorescence images of Ctnna1 localization within the contact plane of control doublets (*Upper*) and doublets exposed to 50 nM LPA (*Lower*) in the last prebleach (*Left*) and first postbleach frames (*Right*). Boxed regions (*Left*) and arrows (*Right*) outline bleached regions. (Scale bar: 10 µm.) (*B*) Normalized intensity kymographs of Ctnna1 recovery after photobleaching at the cell–cell contact edge of control doublets and doublets exposed to 50 nM LPA. (Scale bars: horizontal, 6 s; vertical, 10 µm.) (*C*) Quantification of Ctnna1 fluorescence intensity within the bleached regions at the contact edge of control doublets (purple) and doublets exposed to 50 nM LPA (red) as a function of time after photobleaching. τ denotes the recovery characteristic timescale. Thin lines denote individual cases, and thick lines are averages. (Ctrl) $N = 3$ and $n = 12$; (LPA_{50}) $N = 2$ and $n = 7$. *Materials and Methods* has details. If not stated otherwise, *N* corresponds to the number of experiments, and *n* corresponds to the number of cell doublets.

presence of Jasp exceeds the resistance of the actin cytoskeleton to considerable deformation when pulled into tethers. Importantly, the formation of actin-filled tethers upon separation was not observed when increasing cytoskeletal anchoring (6) of the E-cadherin adhesion complex by LPA, presumably as a result of LPA, but not Jasp, also promoting cortical actomyosin tension resisting actin network deformation.

We then asked how increasing the cortical anchoring strength of the E-cadherin adhesion complex would affect E-cadherin clustering in cell doublets. Analyzing the distribution of Ctnna1 at the contact in Jasp-treated doublets revealed enhanced accumulation at the contact edge (Fig. 4*C*), which was accompanied by similar changes in actin localization (Fig. 4*C*). Myosin II distribution, in contrast, did not show such changes in response to Jasp treatment (Fig. 4*C*). Furthermore, high-resolution analysis of Ctnna1 clustering at the contact edge in Jasp-treated doublets revealed brighter and larger Ctnna1 clusters when the anchoring strength was elevated upon exposure to Jasp (Fig. 4*D*).

Finally, we asked how modulating E-cadherin complex anchoring to the cortex and consequently, E-cadherin clustering at cell–cell contacts would affect cell–cell contact expansion in doublets. To this end, we analyzed contact expansion in doublets exposed to Latr or Jasp, decreasing and increasing anchoring strength, respectively. Strikingly, we found that contact expansion in doublets was strongly reduced not only upon actin destabilization via Latr but also, by stabilizing it in the presence of Jasp (Fig. 4*E*). Together, these findings suggest that cortical tension limits contact expansion by enhancing the anchoring of the cadherin adhesion complex to the actomyosin cortex and as a result of this, cadherin clustering and stability at cell–cell contacts.

Treating progenitor doublets with Latr and Jasp most likely not only affects E-cadherin cortical anchoring strength but also, other cell properties, such as cortical actin network rigidity (16), that might secondarily impact contact formation. To more specifically interfere with E-cadherin cortical anchoring, we therefore turned to truncated and/or fused versions of cadherin that change its ability to couple to the actomyosin network (6, 39, 40). To determine how disrupting cortical anchoring of the cadherin adhesion complex affects cytoskeletal anchoring of the E-cadherin adhesion complex and contact expansion, we substituted the endogenous E-cadherin in progenitors forming doublets with a truncated version of N-cadherin lacking its cytoplasmic tail (Cdh2Δcyto) and thus, its ability to anchor to the cortical actomyosin network (6). We used *N*-cadherin (Cdh2) instead of E-cadherin as expressing sufficient amounts of exogenous Chd2 to substitute for the function of endogenous E-cadherin in germ-layer progenitors turned out to be easier than expressing exogenous E-cadherin (6). We first tested whether the cytoplasmic tail of Cdh2 is required for LPA to promote cadherin anchoring to the actin cortex. When comparing the contact stress of doublets in the presence vs. absence of LPA expressing either full-length Cdh2 (Cdh2FL) or its truncated version (Cdh2Δcyto), we found that LPA increases the contact stress only in doublets expressing Cdh2FL but not Cdh2Δcyto (*SI Appendix*, Fig. S7). This suggests that the cytoplasmic tail of Cdh2 is required for LPA enhancing Cdh2 cytoskeletal anchoring. To further test whether the cytoskeletal anchoring of Cdh2 is needed for LPA restricting contact expansion in doublets, we compared contact expansion in cell doublets expressing either Cdh2FL or Cdh2Δcyto. Strikingly, doublets expressing Cdh2Δcyto failed to show any recognizable changes in contact expansion when exposed to LPA (Fig. 5 and *SI Appendix*, Fig. S8), while doublets expressing Cdh2FL displayed similar changes in contact expansion and size upon LPA treatment (50 nM) to those found in control cell doublets (Fig. 5). Finally, to directly test whether cytoskeletal anchoring of the cadherin adhesion complex restricts contact expansion, we substituted endogenous E-cadherin with a version of Cdh2 where the cytoplasmic tail is replaced by the actin binding domain (ABD) of utrophin (Cdh2△cyto-UtrABD). We found that contact expansion was significantly reduced in doublets expressing Cdh2△cyto-UtrABD compared with those expressing Cdh2FL (Fig. 5), consistent with the notion that anchoring of the cadherin adhesion complex to the actin cytoskeleton inhibits contact expansion. Collectively, these findings strongly suggest that cortical tension restricts contact expansion by promoting the cytoskeletal anchoring of the cadherin adhesion complex.

Discussion

Our findings suggest a nonmonotonic relationship between cell cortex tension and cell–cell contact size. At low and moderate levels of cortical tension, contact size positively scales with tension, consistent with a simple model where the level of cortical tension pulling on the contact edge sets the ratio of interfacial tension at the cell–cell interface (where cortex tension is uniformly and strongly down-regulated) to the cell–medium interface, which again determines the size of the contact after force equilibrium between the contacting cells is reached. At high levels of cortical tension, however, the contact size inversely scales with the level of tension. Importantly, this does not argue against the general concept of force equilibrium between the

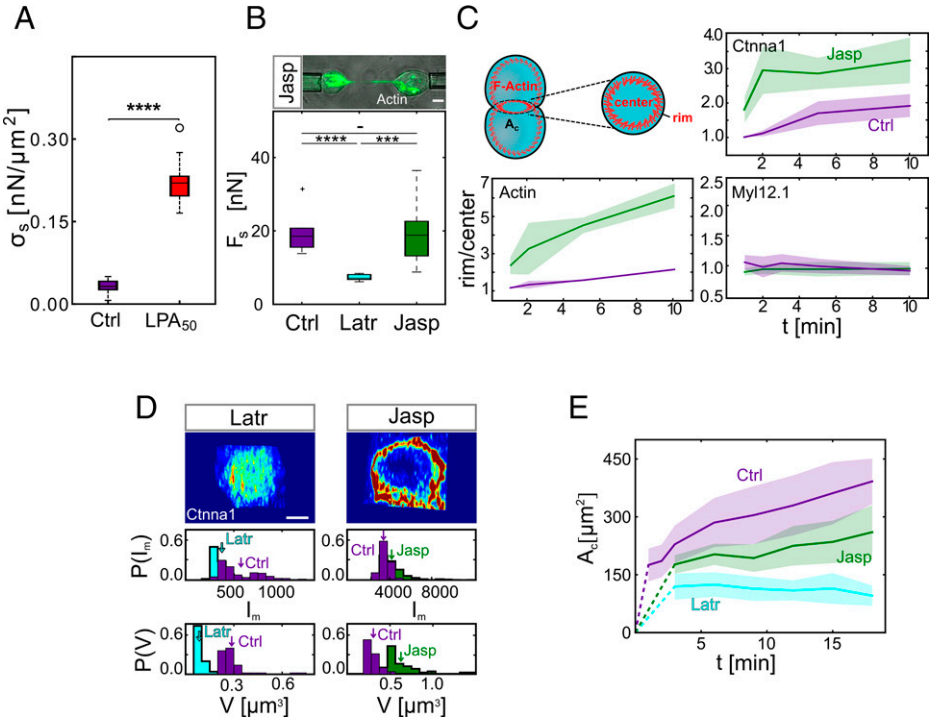

Fig. 4. Enhanced cytoskeletal anchoring of the cadherin adhesion complex by cortical tension limits contact expansion in doublets. (*A*) Contact stress (σ_c) for control progenitor cell doublets and doublets exposed to 50 nM LPA after 10-min contact time. (Ctrl) $N = 13$ and total $n = 17$; (LPA_{50}) $N = 7$ and total $n = 12$. ****P value = 3.6e-17 Student's t test. (*B*) Separation force (F_s) for control doublets and doublets exposed to 300 nM Latr or 100 nM Jasp. *Upper* shows actin-rich tethers formed between the cells during separation in the presence of Jasp. (Ctrl) $N = 3$ and $n = 10$; (Latr) $N = 1$ and $n = 8$; (Jasp) $N = 3$ and $n = 13$. (Ctrl–Jasp) Not significant (t test with Bonferroni correction for multiple comparisons). ***(Latr–Jasp) P value = 6.96e-4; ****(Ctrl–Latr) P value = 1.92e-5. (Scale bar: 5 µm.) (*C*) Rim to center mean intensity ratios for F-actin, myosin II, and Ctnna1 as a function of contact time (1, 2, 5, and 10 min) in the presence or absence of Jasp. F-actin was visualized by Phalloidin with $N = 3$; (Ctrl) $n = 5$, 3, 3, and 3 (corresponding to the different contact times mentioned above); and (Jasp) $n = 3$, 4, 3, and 4. Ctnna1 was visualized by immunohistochemistry with $N = 1$; (Ctrl) $n = 5$, 3, 5, and 5; and (Jasp) $n = 3$, 3, 3, and 4. Myosin II was visualized by Myl12.1-eGFP expression with $N = 1$; (Ctrl) $n = 9$, 8, 7, and 8; and (Jasp) $n = 12$, 9, 11, and 8. The shadowed areas denote SD. (*D*) Exemplary Airy Scan images of Ctnna1 subcellular localization at the contact edge of doublets exposed to Latr or Jasp. Quantifications below show cluster mean intensity (I_m) and volumes (V) of the 50 largest clusters of each cell–cell contact. Arrows indicate distribution means. $N = 1$; (Latr) $n = 7$; and (Jasp) $n = 5$. (Scale bar: 5 µm.) (*E*) Cell–cell contact size (A_c) of control doublets and doublets exposed to Jasp or Latr as a function of contact time. Dotted lines connect contact formation (0 min) with the first time point when data were collected. The shadowed area denotes SD with (Ctrl) N and n as in Fig. 1*C*. (Jasp) $N = 4$, n = (3 min: 6, 6 min: 6, 9 min: 16, 12 min: 16, 15 min: 16, 18 min: 16); (Latr) $N = 4$, n = (3 min: 21, 6 min: 21, 9 min: 21, 12 min: 21, 15 min: 21, 18 min: 9). If not stated otherwise, N corresponds to the number of experiments, and n corresponds to the number of cell doublets.

contacting cells determining contact size (note that the LPA-treated contacts still slowly expand up to the longest experimentally still accessible contact times) (Fig. 1*C*) but rather, suggests that the ability of the contact to expand might be force sensitive, permitting fast contact expansion at low to moderate levels of cortical tension while considerably slowing it down at high tension levels.

We also show that cortical tension diminishes the ability of the contact to expand by increasing E-cadherin anchoring to the cortical actomyosin cytoskeleton and that this enhanced anchoring leads to E-cadherin clustering and reduced turnover of the E-cadherin adhesion complex at the contact. Previous studies have provided evidence that unfolding of α-catenin and stabilization of the actin network are involved in mediating the effect of tension on E-cadherin clustering by promoting cytoskeletal anchoring of the cadherin adhesion complex (16, 20, 21, 36, 41, 42). Our observations suggest not only that cortical tension triggers those mechanosensitive effector processes but that activation of those processes has severe morphogenetic consequences by restricting contact expansion and enhancing contact strength. Notably, while our findings are consistent with a critical role of mechanosensation at the level of α-catenin to actin binding in mediating the effect of increased cortical tension on limiting contact expansion, it does not exclude other potentially contributing processes, such as changes in cortical actomyosin network stiffness as a result of contraction (43). To what extent those alternative mechanisms might affect the nonmonotonic relationship between cortical tension and contact size, however, still needs to be explored.

Commonly, contact size is assumed to scale with contact strength, and there are multiple cases where such a relationship has been documented (6, 12, 44). Our findings of an inverse relationship between contact size and strength point at the possibility that some processes might benefit from cell–cell contacts being simultaneously small and strong. For instance, during collective or chain cell migration, cells need to establish stable contacts with their neighbors and at the same time, retain contact-free interfaces that allow them to form protrusions required for cell migration (45, 46). This points at the possibility that the nonmonotonic coregulation of contact size and strength as a function of cortical tension might reflect specific features of these contacts; at low to moderate levels of cortical tension, contact size might be less important as contacts are likely to be more transient and flexible. At high cortical tension, in contrast, contacts are expected to be long lived and stable, and thus, contact size will more permanently affect other processes requiring cell–cell contact-free interfaces, such as cell protrusion formation and cell matrix adhesion. Whether and how the combined effect of contact size and strength affects specific biological processes remain to be investigated.

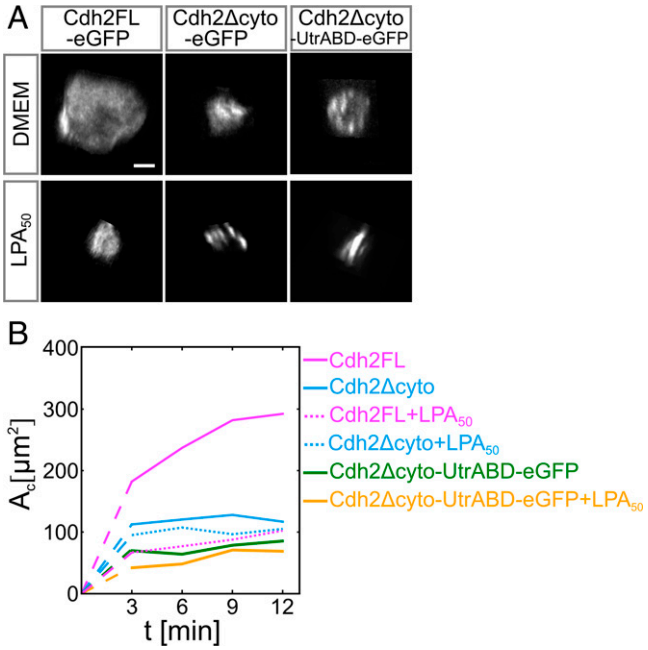

Fig. 5. Defective cytoskeletal anchoring of the cadherin adhesion complex suppresses the effect of cortical tension on contact expansion. (*A*) Subcellular localization of Cdh2FL-eGFP, Cdh2Δcyto-eGFP, and Cdh2Δcyto-UtrABD-eGFP at the contact of doublets in the presence or absence of 50 nM LPA. (Scale bar: 5 μm.) (*B*) Cell–cell contact size (A_c) in doublets expressing either Cdh2FL (pink), Cdh2Δcyto (blue), or Cdh2Δcyto-UtrABD-eGFP (green and yellow) in the presence (dotted lines, yellow for Cdh2Δcyto-UtrABD-eGFP) or absence (solid lines, green for Cdh2Δcyto-UtrABD-eGFP) of 50 nM LPA. Dashed lines connect contact formation (0 min) with the first time point when data were collected. SDs are shown in *SI Appendix*, Fig. S8. (Cdh2FL) $N = 2$, $n =$ (3 min: 8, 6 min: 8, 9 min: 8, 12 min: 8); (Cdh2Δcyto) $N = 2$, $n =$ (3 min: 14, 6 min: 14, 9 min: 14, 12 min: 14); (Cdh2Δcyto + LPA_{50}) $N = 2$, $n =$ (3 min: 9, 6 min: 9, 9 min: 9, 12 min: 9); (Cdh2FL + LPA_{50}) $N = 2$, $n =$ (3 min: 10, 6 min: 10, 9 min: 10, 12 min: 10); (Cdh2Δcyto-UtrABD-eGFP) $N = 3$, $n =$ (3 min: 5, 6 min: 5, 9 min: 5, 12 min: 5); (Cdh2Δcyto-UtrABD-eGFP + LPA_{50}) $N = 1$, $n =$ (3 min: 3, 6 min: 3, 9 min: 3, 12 min: 3). If not stated otherwise, *N* corresponds to the number of experiments, and *n* corresponds to the number of cell doublets.

There is manifold evidence for cadherin-mediated cell–cell contacts being mechanosensitive (47, 48). While the molecular and cellular mechanisms underlying this mechanosensitivity have been studied in detail (6, 49, 50), comparably little is yet known about its function in contact formation and maintenance. Our findings of an important function for mechanosensation at cadherin-mediated cell–cell contacts in controlling contact expansion identify a yet unknown role of mechanosensation in determining contact dynamics and strength.

Materials and Methods

Fish Lines and Husbandry. Zebrafish maintenance was carried out as described (51). Embryos were grown at 28 to 31 °C in embryo medium (E3) (5 mM NaCl, 0.17 mM KCl, 0.33 mM CaCl, 20.33 mM $MgSO_4$) and prior to experiments, dechorionated in Danieau's embryo medium [58 mM NaCl, 700 μM KCl, 400 μM $MgSO_4$, 600 μM $Ca(NO_3)_2$, 5 mM 4-(2-hydroxyethyl)-1-piperazineethanesulfonic acid (Hepes) at pH 7.2]. Embryos were staged based on morphological criteria (52). The following fish lines were used; wild-type embryos were obtained from the Tup-Longfin (TL) and Pet Shop A × Pet Shop B (AB) background; transgenic fish lines used were Tg(*ctnna-citrine*)^{ct3a} (53), Tg(*bAct:myl12.1-eGFP*) (6), Tg(*bAct:myl12.1-mCherry*) (6), Tg(*bAct:LifeAct-eGFP*) (5), and Tg(*actb1: mCherry–utrCH*) (39).

Cell Culture. To prepare primary cultures of zebrafish progenitor cells for live imaging, embryos consisting of ectoderm cells only (see *mRNA and* morpholino *Injections*) were raised as described above. After embryo dechorionation in Danieu's medium at sphere stage (4 h postfertilization [hpf]), the blastoderm cap was dissected from the yolk cell using forceps and transferred first to CO_2—independent Dulbecco's modified Eagle medium: nutrient mixture F-12 culture medium (DMEM/F12; Invitrogen; complemented with L-Glut, 15 mM Hepes, and 100 U/mL penicillin plus streptomycin, adjusted at pH 7.5, sterilized using 0.45-μm pore filters, and preheated to 28 °C)—and then to an Eppendorf tube containing 200 μL culture medium using a glass pipette. Blastoderm caps were afterward mechanically dissociated into single cells by gentle tapping on the tube, and the cells were then transferred into a fetal bovine serum (FBS; Gibco)–coated glass-bottom dish (MatTek glass-bottom dish, 35 mm; MatTek Corporation). Cell–cell contact formation was initiated by gently bringing two cells together using micropipettes (6, 9), and the newly formed cell doublet was imaged up to 20 min.

mRNA and *morpholino* Injections. Zebrafish embryos were induced to consist of ectoderm progenitors only by microinjection of one cell–stage embryos with 100 pg *lefty1* messenger RNA (mRNA). To substitute endogenous E-cadherin with controlled amounts of full-length or truncated Cdh2, 8 ng *e-cadherin/cdh1 morpholino* (5′-TAAATCGCAGCTCTTCCTTCCAACG-3′; GeneTools) together with either 100 pg of *cdh2FL-eGFP*, 100 pg of *cdh2Δcyto-eGFP*, or 100 pg of *cdh2Δcyto-UtrABD-eGFP* mRNA (6, 54) was injected into one cell–stage embryos. To increase cortical tension, 5 pg of *ca RhoA* (28) and to visualize subcellular vinculin distribution, 150 pg of *vinculinB-eGFP* were injected into one cell–stage embryos. The cell membrane was labeled by injection of 50 to 100 pg membrane-bound red fluorescent protein. The covisualization of Ctnna1 with vinculin was done by injecting 100 pg of *ctnna1-mcherry* (6) and 100 pg of *vinculinB-eGFP*. Synthetic mRNA was produced by using the SP6 mMesage mMachine kit (Ambion).

Immunostaining. Single progenitor cells were obtained as described in *Cell Culture* and allowed to seed on MatTek dishes for 30 min. Cells were then fixed with 4% paraformaldehyde (PFA; Sigma-Aldrich) in DMEM/F12 for 10 min at room temperature (RT), washed three times with phosphate buffered saline (PBS; Sigma-Aldrich) to remove the PFA, and incubated in phosphate buffered saline with 0.3% Triton ×100 (PBT; Merck) for 30 min at RT to permeabilize the plasma membrane. PBT was subsequently replaced with blocking solution consisting of PBT with 1% dimethyl sulfoxide (Sigma-Aldrich) and 10% goat serum (Gibco) for 1 h at RT before primary antibodies diluted in blocking solution were added overnight at 4 °C. Cells were washed three times with PBS at RT, and secondary antibodies diluted in blocking solution were added for 2 h at RT, followed by three washes with PBS at RT to remove the antibodies. The following primary antibodies were used: αE-catenin (1:1,000; Sigma-Aldrich; C2081), Vinculin (1:100; Sigma-Aldrich; V4505), and E-cadherin [1:250; MPI-CBG (55)]. As secondary antibodies, fluorescently Alexa-488–, Alexa-647–, or Alexa-568–coupled secondary antibodies (1:250; Molecular Probes) were used. For labeling F-actin, Phalloidin (1:250; Invitrogen) was used. Immunolabeled cells were imaged on a Zeiss Observer inverted microscope equipped with a Spinning Disk System (see *Imaging Acquisition*).

Imaging Acquisition. Fluorescence imaging of cells was performed on the Spinning Disk System (Andor Revolution Imaging System; Yokogawa CSU-X1) placed on an inverted microscope (Axio Observer Z1 Zeiss) using a 40×/1.2 numerical aperture (NA) water immersion lens (Zeiss) for time-lapse imaging and a 100×/1.4 NA oil (Zeiss) for still images. The setup was equipped with a motorized piezo stage, stage heating, and objective heater units. Single- and dual-color fluorescence images were acquired using 488- and 561-nm laser lines with an optical slicing of 0.5 μm; 30-mW maximum laser output power was used, and images were acquired using an iXon DU-897-BV electron-multiplying CCD (EMCCD) camera (Andor Technology) with exposure times set to 100 to 300 ms and frame rates between 1 and 2 s. Resulting image *z* stacks were rotated using Imaris 9.1.2 (Bitplane) to obtain cross-sections of cell–cell contacts between cell doublets. High-resolution images of endogenous E-cadherin/Cdh1, Ctnna1, and F-actin clusters were obtained using an inverted Zeiss LSM 880 confocal/"Airy Scan" using a 63×/1.4 NA oil (Zeiss), and image analysis was performed using ImageJ software (56).

Image Analysis. Visualization of Ctnna1 clusters was performed using deconvolved (Zeiss ZEN 2.3) *z* stacks of confocal images of cell doublets, with 50 to 100 images per stack and 0.19-μm *z* increment. Protein cluster volume and fluorescence intensity were detected and quantified following ref. 57, using Imaris 9.1.2 (Bitplane). VinculinB-GFP fluorescence intensity was quantified from z-stack images of cell–cell contacts by first selecting a plane in the stack, where the cell–cell contact appeared the largest (corresponding to the middle of the contact), and then measuring average intensity in two 3 × 3-pixel regions located at the edges of the cell–cell contact (rim intensity) and two in the middle of the contact line (center intensity). From that, rim to center ratio was calculated.

FRAP. For each experiment, two progenitor cells from the Tg(*ctnna-citrine*)^{ct3a} line were placed in a polymer well mounted on a MatTek dish using pipettes and allowed to form a contact. Subsequently, the cell–cell contact plane was aligned with the focal plane. After cells had been in contact for 10 ± 2 min, at least 10 frames of prebleach fluorescence intensity were recorded, and then, a 488 laser (300 pulses, 300 ms, dwell time 30 μs) was used to bleach a small rectangular area on the contact edge (region of interest) with the size of 8×8 pixels. Imaging of the bleached area was performed at 3.3 frames/s with an image size of 512×512 pixels for at least 60 s before the contact plane would typically drift out of the focal plane.

For each bleached contact, a polar transformation was performed around the center of the contact for a prebleach image followed by a postbleach image series (300 ms from the recorded time series) using the ImageJ Polar Transformer plug-in (https://imagej.nih.gov/ij/plugins/polar-transformer.html). In the transformed images, a line profile was taken along the contact edge (line thickness: nine pixels), and the radial span of the bleached region was recorded. Subsequent stacks were aligned into kymographs using a cross-correlation method to correct for cell doublet rotation. The intensity in the bleached region $I_b(t)$ and that outside of it $I_u(t)$ were then recorded over time. To correct for acquisition photobleaching, the following transformations were applied to the data:

$$f(t) = I_u(t)/I_b(t)$$
$$g(t) = 1 - f(t)$$
$$h(t) = g(t)/g(t = 0),$$

where $t = 0$ corresponds to the first time point after bleaching. In this way, $h(t) \to 0$ corresponds to full recovery of the signal. Single exponential recovery equations were then fitted using nonlinear least squares to $h(t) = e^{-\tau \times t}$, where τ is the characteristic recovery time. Fitting errors were calculated as squares of diagonal elements of the covariance matrix. In Fig. 3*C*, $h(t) = 1 - 1/h(t)$ is shown to conform to typical representation of the FRAP data.

Rim to Center Ratio and Contact Size Analysis. A number of freshly formed cell doublets (typically one to four) expressing citrine-tagged Ctnna1 were followed for up to 20 min (at which point the cells would typically drift from the field of view or divide) and imaged every 3 min on a spinning-disk microscope using *z* stacks. From each doublet, three substacks were cut out for every time point: one containing the cell–cell contact with thickness d and two stacks containing small cytosol volumes from each cell, from which the average cytosolic signal intensity (I_c) was calculated. Subsequently, the cell–cell contact was projected on a plane (sum of the signal), and background signal $I_c \times d$ was subtracted from it. The contour of the contact was detected by applying a combination of thresholding (typically at the 1.5 to 2.5 times background intensity, visually assessed to contain whole cell–cell contacts) and subsequent dilation of the binarized image to account for uneven distribution of adhesion molecules at the cell–cell contact rim. An ellipse was then fitted to the contour using a set of custom-made scripts in order to calculate the surface area $C_c = \pi \times a \times b$, where a and b denote ellipse semiaxes. Due to the dotted and discontinuous nature of the GFP signal in cells expressing Cdh2FL, Cdh2Δcyto, and Cdh2Δcyto-UtrABD the automatic contact size measurement was not possible. In these cases, the diameter of each cell–cell contact was manually measured using ImageJ.

Integrated Intensity Analysis. Cell doublets were placed in polymer wells as described above, with cell–cell contacts selected that had the contact plane well aligned with the imaging plane. Background values were taken as average fluorescence intensity in a neighboring empty polymer well and subtracted from each image. Cell–cell contacts were outlined, and the sum of the raw fluorescence intensity was calculated.

Dual-Pipette Assay. Single progenitor cells were prepared as described in *Cell Culture*. MatTek glass-bottom dishes were passivated by incubation in heat-passivated FBS (Invitrogen) for at least 20 min at RT. Glass pipettes with a diameter of 8 μm (Biomedical Instruments) were passivated in the same way for 7 min, washed with PBS, and connected to a Microfluidic Flow Control System (Fluigent; Fluiwell) with negative pressure range of 7 to 750 Pa, accuracy of 7 Pa, and change rate of 200 Pa/s on two independent channels. Micropipette movement was performed by micromanipulators (Eppendorf; Transferman Nk2), which together with the pressure, were controlled via a custom-programmed Labview (National Instruments) interface. Dissociated cells from one to two embryos were transferred to the MatTek dishes in 4 mL DMEM/F12 and allowed to seed for at least 10 min. To manipulate single cells, ∼20-Pa negative pressure in the pipettes was used.

For each measurement, two healthy-looking cells were selected, put in contact, and left unperturbed for 10 min. Afterward, both cells were aspirated by pipettes, and the negative pressure in one of the pipettes (holding pipette) was adjusted to hold one cell firmly. The pressure in the other pipette was then increased in a stepwise fashion, and at each step, a separation attempt was performed, which involved moving the pulling pipette away from the holding pipette with a constant speed of 20 μm/s up to a distance of 20 μm. Pressure was recorded at each separation attempt, and subsequently, separation force (F_s) was calculated according to the equation

$$F_s = \pi {R_p}^2 (P_{k-1} + P_k)/2,$$

where R_p is the pulling pipette radius, $k = 1, 2, \ldots$ is the attempt number, and P_{k-1} and P_k are pressure values in the last unsuccessful and the first successful separation attempt, respectively. Experiments where more than six attempts were needed for separation were excluded from the study to avoid mechanosensitive stiffening of the separated cells.

Triplet Assay. Cell culture was prepared as described above. Linear cell triplets of 50 nM LPA-treated and untreated cells were arranged using micropipettes and allowed to expand their contacts for 5 to 8 min. Central cell radius was measured three times prior to separation. Flanking cells were then aspirated, and triplets were separated by pulling one of the pipettes away from the triplet. After separation, movies were recorded tracking the bulge formed on the central cell of the triplet in the place of the former contact. Bulge radius measured by connecting the edges of the bulge by a straight line and taking half of the line length three times for each triplet. The ratio of the bulge radius to the central cell radius was then plotted, yielding the ratio of cortical tensions at the cell–medium to the cell–cell interfaces (6).

Transmission Electron Microscopy. For high-pressure freezing of cells, sapphire disks of 1.4×0.05 mm in diameter (Wohlwend) were carbon coated to a thickness of 10 nm using the Leica EM ACE600 high-vacuum coating device (Leica Microsystems). The pattern of a Maxtaform H15 finder grid (Science Services; LF 135-Ni) was evaporated onto the disk surface, and the coat was stabilized by baking overnight at 120 °C. After plasma cleaning for 2 min (Harrick plasma cleaner; radio frequency level medium), sapphire disks were incubated overnight at 4 °C in 10 μM solution of Concavalin A (Sigma-Aldrich) and washed thoroughly in PBS. They were then placed into cup-shaped aluminum planchettes with cavity dimensions of 2-mm inner diameter and 100-μm indentation (Wohlwend). Primary progenitor cells were prepared as described in *Cell Culture* above and plated onto the sapphires with cells from one embryo on average distributed over two disks. Cells were allowed to form spontaneous contacts and adhere to the disk surface for 10 min at RT. One microliter of 5% bovine serum albumin (BSA) (Sigma-Aldrich; A-9647) in medium equilibrated to RT was then added as a space filler and antifreezing agent. The flat side of an aluminum planchette with a 300-μm indentation was used as a lid, and excess of solution was removed with filter paper. The sandwiched samples were high-pressure frozen instantaneously using the HPM-010 high-pressure freezing machine (Leica Microsystems), transferred to cryovials (Biozym; T311-2), and then stored in liquid nitrogen.

For freeze substitution, samples were processed in an AFS1 device (Leica Microsystems) with ethanol in the loading chamber. Two substitution mixtures were applied consecutively: 1) 1% tannic acid (Sigma-Aldrich; 403040) in nonhydrous acetone (VWR; 8.22251) and 2) 1% osmium (EMS; 19134) plus 0.2% uranyl acetate (20% stock in methanol; AL-Labortechnik; 77870.2) in nonhydrous acetone. Two-milliliter screw-cap Nalgene cryovials (Sigma-Aldrich; V4632) were used for substitution filled with 1 mL of mixture. The sequence for infiltration and stepwise warming was as follows: 24 h of incubation in 0.1% tannic acid in acetone at −82 °C, three 10-min washes in acetone at −82 °C, 6 h of incubation in 1% osmium plus 0.2% uranyl acetate in acetone at −82 °C, temperature rise of 15 °C/h to −60 °C, 3 h of incubation at −60 °C, temperature rise of 15 °C/h to −30 °C, 3 h of incubation at −30 °C, three 10-min washes in acetone at −30 °C, and temperature rise of 15 °C/h to 4 °C. Sapphires were then removed from the aluminum planchettes and embedded in epoxy resin (Durcupan ACM; Fluca). Samples were consecutively infiltrated with a 3:1 mixture of acetone and Durcupan for 1 h at 4 °C, 1:1 acetone/Durcupan for 1.5 h at 4 °C, 1:3 acetone/Durcupan for 2 h at 4 °C, and mere Durcupan overnight at RT. Samples were transferred to BEEM capsules (EMS; 70020-B) filled with freshly prepared Durcupan and cured for 48 h at 60 °C in an oven. Serial ultrathin sections (70 to 80 nm) were cut using an UC7 ultramicrotome (Leica Microsystems) and collected onto formvar-coated copper slot grids. The sections were then contrast enhanced by incubating them in 1% aqueous uranyl acetate for 10 min at RT and Reynold's lead citrate for 2 min at RT.

Sections were examined in a Tecnai 10 transmission electron microscope (Thermo Fisher Scientific) operated at 80 kV and equipped with an EMSIS

side-mounted camera Megaview III. Images were processed with Radius software (EMSIS) and Photoshop (Adobe) without changing any specific feature. For high-resolution analysis, sections were examined in a JEM 2800 scanning transmission electron microscope (Jeol) operated at 200 kV in STEM bright-field mode and equipped with a side-mounted OSIS Veleta camera (EMSIS).

CLEM. Disks of 1 cm in diameter were cut from Aclar foil (thickness: 198 μm; TedPella; 10501-10) and placed in sterile Corning 12-well plates (Sigma-Aldrich; CLS 3737). Dissociated cells were plated on the these disks (cells from one blastoderm per disk), and they were allowed to form spontaneous cell–cell contacts and adhere to the disk surface for 10 min at RT. Cells were then fixed with 4% PFA (Sigma-Aldrich; 158127) in PBS (pH 7.4) for 10 min at RT and washed three times with PBS. Subsequently, Phalloidin conjugated with Alexa-488 (Invitrogen; 1/250 in PBT) was applied to the cells for 3 h at RT to label F-actin. In an additional round of fixation, 4% PFA plus 0.05% glutaraldehyde (Agar Scientific; R1020) in PBS was applied for 20 min at RT. After washing in PBS, 50 mM glycine (VWR; 24403.298) in PBS was used to block free aldehyde groups for 20 min at RT. After washing in PBS again, samples were dehydrated in graded ethanol (50, 70, 90, 96, 100%) and embedded in LR-White resin (Sigma-Aldrich; 62661). Samples were consecutively infiltrated with a 1:1 mixture of ethanol to LR-White, 1:2 ethanol/LR-White, and mere LR-White for 20 min each at 4 °C. Samples were transferred to gelatin capsules (Science Services; 70103), filled with fresh LR-White, capped tightly, and cured for 12 h at 50 °C in an oven. Sections were cut at 180 nm and mounted on 15-mm glass coverslips coated with a Tissue Capture Pen (EMS; 71314-10). Sections were then embedded in VectaShield (Vector Laboratories), coverslipped, and imaged under an LSM 880 microscope (Zeiss) with an oil immersion objective (40× NA 1.4) using an Airy Scan detector. Overview images were taken to facilitate localization of doublets on the section. After fluorescence imaging, coverslips were removed from glass slides, and sections were contrast enhanced by incubating them in 1% aqueous uranyl acetate for 10 min at RT and Reynold's lead citrate for 4 min at RT. Sections were then observed under a Merlin VP Compact FE-Scanning Electron Microscope (Zeiss) using an In-Lens Duo detector (In-Lens SE and In-Lens BSE). Images from details were first aligned to the overviews, where the whole cell–cell doublet was visible using the SIFT algorithm (58). Subsequently, fluorescent images were aligned with the EM overviews using the easy cell–CLEM method (59) implemented in Icy open-source software (40).

AFM. Cell cortex tension measurements on single cells were performed as described previously (29), with preparation of single cells as described in *Cell Culture*. For each experiment, individual cells from five blastoderm preparations were seeded on a tissue culture dish with a cover glass bottom (FluoroDish) containing DMEM/F12 either alone (control) or complemented with 5 or 50 nM LPA or 10 μM Bb. Cells were probed using AFM (NanoWizard 4 BioScience; JPK Instruments; mounted on an inverted fluorescent microscope [Olympus IX71]). Commercial colloidal force probes (CP-qp-CONT-BSA-A; NanoAndMore USA) were passivated with heat-inactivated fetal calf serum (FCS; Invitrogen) for 1 h at RT to avoid nonspecific adhesion of the bead to the cells. Force distance curves were acquired using 500-pN contact force and 1-μm s^{-1} approach/retract velocity. Up to three curves with 10-s waiting time between successive curves were taken per cell to prevent any history effect. Indentation was calculated from the tip displacement. To obtain the values of cell cortex tension, the liquid droplet model was applied as described previously (29), with the following adjustments; for determining cell cortex tension, a force vs. indentation line fit between the 200- and 300-nm indentation range was applied.

Reagents and Inhibitors. Fetal BSA (GIBCO), heat-passivated FBS (Invitrogen), heat-inactivated FCS (Invitrogen), and 1-oleoyl LPA (Tocris Bioscience) were used at the indicated concentrations (1, 5, 10, and 50 nM). Pharmacological inhibitors were used at the following concentrations: 10 μM active (−) or inactive (+) Bb (Tocris Bioscience), 0.3 μM Latrunculin-B (Sigma-Aldrich), 100 nM Jasp (Invitrogen), and 2 mg/mL Concavalin A (Sigma-Aldrich).

Polymer Microwell Preparation. To facilitate imaging of the cell–cell contacts in the focal plane, a microwell setup was used as described (16). In order to ascertain that the cell doublet will always remain in the correct position during the experiment, microwells with a range of well diameters (15 to 30 μm) and 50-μm depth were prepared. Polydimethylsiloxane (PDMS) stamps containing the negative of the desired pattern were gently pressed to droplets of My Polymer 134 (My Polymers) applied to Mattek glass-bottom petri dishes and then, ultraviolet (UV) curated (Thorlabs UV light-emitting diode 365 nm) in nitrogen atmosphere for up to 1 h, at which point the PDMS stamps were peeled off.

Statistical Analysis and Repeatability of Experiments. Statistical analyses of data were performed using the GraphPad Prism 6 software and the statsmodel python package. Statistical details of experiments are reported in the figures. To test for normality of a sample, a D'Agostino and Pearson omnibus normality test was used. In case two samples were compared and normal distribution was assumed, an unpaired *t* test was performed, while the Mann–Whitney test was performed in case of not normally distributed data. In case more than two normally distributed samples were compared, an ANOVA was performed followed by Tukey's multiple comparison test. Alternatively, the Student's *t* test was performed with Bonferroni correction for multiple comparisons as stated in detail in the figures. If no normal distribution could be assumed, a Kruskal–Wallis test followed by Dunn's multiple comparison test was used. At least more than three independent experiments (*N*) were performed unless stated otherwise in the figures. No statistical method was used to predetermine sample size, the experiments were not randomized, and the investigators were not blinded to allocation during experiments and outcome assessment. *P* value of <0.05 was considered as significant.

Data Availability. All study data are included in the article and/or *SI Appendix*.

ACKNOWLEDGMENTS. We thank Guillaume Salbreaux, Silvia Grigolon, Edouard Hannezo, and Vanessa Barone for discussions and comments on the manuscript and Shayan Shamipour and Daniel Capek for help with data analysis. We also thank the Imaging & Optics, Electron Microscopy, and Zebrafish Facility Scientific Service Units at the Institute of Science and Technology Austria (ISTA)Nasser Darwish-Miranda for continuous support. We acknowledge Hitoshi Morita for the gift of VinculinB-GFP plasmid. This research was supported by an ISTA Fellow Marie-Curie Co-funding of regional, national, and international programmes Grant P_IST_EU01 (to J.S.), European Molecular Biology Organization Long-Term Fellowship Grant, ALTF reference number: 187-2013 (to M.S.), Schroedinger Fellowship J4332-B28 (to M.S.), and European Research Council Advanced Grant (MECSPEC; to C.-P.H.).

1. C. Yoshida, M. Takeichi, Teratocarcinoma cell adhesion: Identification of a cell-surface protein involved in calcium-dependent cell aggregation. *Cell* **28**, 217–224 (1982).
2. S. Hong, R. B. Troyanovsky, S. M. Troyanovsky, Cadherin exits the junction by switching its adhesive bond. *J. Cell Biol.* **192**, 1073–1083 (2011).
3. L. Hinck, I. S. Näthke, J. Papkoff, W. J. Nelson, Dynamics of cadherin/catenin complex formation: Novel protein interactions and pathways of complex assembly. *J. Cell Biol.* **125**, 1327–1340 (1994).
4. D. L. Rimm, E. R. Koslov, P. Kebriaei, C. D. Cianci, J. S. Morrow, Alpha 1(E)-catenin is an actin-binding and -bundling protein mediating the attachment of F-actin to the membrane adhesion complex. *Proc. Natl. Acad. Sci. U.S.A.* **92**, 8813–8817 (1995).
5. A. Nagafuchi, S. Ishihara, S. Tsukita, The roles of catenins in the cadherin-mediated cell adhesion: Functional analysis of E-cadherin-alpha catenin fusion molecules. *J. Cell Biol.* **127**, 235–245 (1994).
6. J.-L. Maître *et al.*, Adhesion functions in cell sorting by mechanically coupling the cortices of adhering cells. *Science* **338**, 253–256 (2012).
7. J.-L. Maitre, C.-P. Heisenberg, Three functions of cadherins in cell adhesion. *Curr. Biol.* **23**, R626–R633 (2013).
8. M. S. Steinberg, Differential adhesion in morphogenesis: A modern view. *Curr. Opin. Genet. Dev.* **17**, 281–286 (2007).
9. R. Winklbauer, Cell adhesion strength from cortical tension—An integration of concepts. *J. Cell Sci.* **128**, 3687–3693 (2015).
10. J. C. Stachowiak *et al.*, Membrane bending by protein-protein crowding. *Nat. Cell Biol.* **14**, 944–949 (2012).
11. T. D. Perez, M. Tamada, M. P. Sheetz, W. J. Nelson, Immediate-early signaling induced by E-cadherin engagement and adhesion. *J. Biol. Chem.* **283**, 5014–5022 (2008).
12. S. Yamada, W. J. Nelson, Localized zones of Rho and Rac activities drive initiation and expansion of epithelial cell-cell adhesion. *J. Cell Biol.* **178**, 517–527 (2007).
13. P. Z. Anastasiadis *et al.*, Inhibition of RhoA by p120 catenin. *Nat. Cell Biol.* **2**, 637–644 (2000).
14. N. Borghi *et al.*, E-cadherin is under constitutive actomyosin-generated tension that is increased at cell-cell contacts upon externally applied stretch. *Proc. Natl. Acad. Sci. U.S.A.* **109**, 12568–12573 (2012).
15. M. Roh-Johnson *et al.*, Triggering a cell shape change by exploiting preexisting actomyosin contractions. *Science* **335**, 1232–1235 (2012).
16. W. Engl, B. Arasi, L. L. Yap, J. P. Thiery, V. Viasnoff, Actin dynamics modulate mechanosensitive immobilization of E-cadherin at adherens junctions. *Nat. Cell Biol.* **16**, 587–594 (2014).
17. C. D. Buckley *et al.*, Cell adhesion. The minimal cadherin-catenin complex binds to actin filaments under force. *Science* **346**, 1254211 (2014).
18. J. Y. Sim *et al.*, Spatial distribution of cell-cell and cell-ECM adhesions regulates force balance while main-taining E-cadherin molecular tension in cell pairs. *Mol. Biol. Cell* **26**, 2456–2465 (2015).

19. J. M. Leerberg *et al.*, Tension-sensitive actin assembly supports contractility at the epithelial zonula adherens. *Curr. Biol.* **24**, 1689–1699 (2014).
20. W. A. Thomas *et al.*, α-Catenin and vinculin cooperate to promote high E-cadherin-based adhesion strength. *J. Biol. Chem.* **288**, 4957–4969 (2013).
21. S. Yonemura, Y. Wada, T. Watanabe, A. Nagafuchi, M. Shibata, alpha-Catenin as a tension transducer that induces adherens junction development. *Nat. Cell Biol.* **12**, 533–542 (2010).
22. R. Desai *et al.*, Monomeric α-catenin links cadherin to the actin cytoskeleton. *Nat. Cell Biol.* **15**, 261–273 (2013).
23. S. Hirano, N. Kimoto, Y. Shimoyama, S. Hirohashi, M. Takeichi, Identification of a neural alpha-catenin as a key regulator of cadherin function and multicellular organization. *Cell* **70**, 293–301 (1992).
24. M. Yao *et al.*, Force-dependent conformational switch of α-catenin controls vinculin binding. *Nat. Commun.* **5**, 4525 (2014).
25. S. Huveneers *et al.*, Vinculin associates with endothelial VE-cadherin junctions to control force-dependent remodeling. *J. Cell Biol.* **196**, 641–652 (2012).
26. Q. le Duc *et al.*, Vinculin potentiates E-cadherin mechanosensing and is recruited to actin-anchored sites within adherens junctions in a myosin II-dependent manner. *J. Cell Biol.* **189**, 1107–1115 (2010).
27. G. B. Mills, W. H. Moolenaar, The emerging role of lysophosphatidic acid in cancer. *Nat. Rev. Cancer* **3**, 582–591 (2003).
28. A. Takesono *et al.*, Solute carrier family 3 member 2 (Slc3a2) controls yolk syncytial layer (YSL) formation by regulating microtubule networks in the zebrafish embryo. *Proc. Natl. Acad. Sci. U.S.A.* **109**, 3371–3376 (2012).
29. M. Krieg *et al.*, Tensile forces govern germ-layer organization in zebrafish. *Nat. Cell Biol.* **10**, 429–436 (2008).
30. P.-H. Puech, K. Poole, D. Knebel, D. J. Muller, A new technical approach to quantify cell-cell adhesion forces by AFM. *Ultramicroscopy* **106**, 637–644 (2006).
31. E. Panther *et al.*, The influence of lysophosphatidic acid on the functions of human dendritic cells. *J. Immunol.* **169**, 4129–4135 (2002).
32. S. Rakshit, S. Sivasankar, Biomechanics of cell adhesion: How force regulates the lifetime of adhesive bonds at the single molecule level. *Phys. Chem. Chem. Phys.* **16**, 2211–2223 (2014).
33. M. Cavey, M. Rauzi, P.-F. Lenne, T. Lecuit, A two-tiered mechanism for stabilization and immobilization of E-cadherin. *Nature* **453**, 751–756 (2008).
34. B.-A. Truong Quang, M. Mani, O. Markova, T. Lecuit, P. F. Lenne, Principles of E-cadherin supramolecular organization in vivo. *Curr. Biol.* **23**, 2197–2207 (2013).
35. G. R. Kale *et al.*, Distinct contributions of tensile and shear stress on E-cadherin levels during morphogenesis. *Nat. Commun.* **9**, 5021 (2018).
36. S. Dufour, R.-M. Mège, J. P. Thiery, α-catenin, vinculin, and F-actin in strengthening E-cadherin cell-cell adhesions and mechanosensing. *Cell Adhes. Migr.* **7**, 345–350 (2013).
37. J. M. Bianchini *et al.*, Reevaluating αE-catenin monomer and homodimer functions by characterizing E-cadherin/αE-catenin chimeras. *J. Cell Biol.* **210**, 1065–1074 (2015).
38. G. Salbreux, G. Charras, E. Paluch, Actin cortex mechanics and cellular morphogenesis. *Trends Cell Biol.* **22**, 536–545 (2012).
39. M. Behrndt *et al.*, Forces driving epithelial spreading in zebrafish gastrulation. *Science* **338**, 257–260 (2012).
40. C. S. Chen *et al.*, α-Catenin-mediated cadherin clustering couples cadherin and actin dynamics. *J. Cell Biol.* **210**, 647–661 (2015).
41. C. Bertocchi *et al.*, Nanoscale architecture of cadherin-based cell adhesions. *Nat. Cell Biol.* **19**, 28–37 (2017).
42. S. Hong, R. B. Troyanovsky, S. M. Troyanovsky, Binding to F-actin guides cadherin cluster assembly, stability, and movement. *J. Cell Biol.* **201**, 131–143 (2013).
43. G. H. Koenderink *et al.*, An active biopolymer network controlled by molecular motors. *Proc. Natl. Acad. Sci. U.S.A.* **106**, 15192–15197 (2009).
44. C. Bertet, L. Sulak, T. Lecuit, Myosin-dependent junction remodelling controls planar cell intercalation and axis elongation. *Nature* **429**, 667–671 (2004).
45. C. Collins, W. J. Nelson, Running with neighbors: Coordinating cell migration and cell-cell adhesion. *Curr. Opin. Cell Biol.* **36**, 62–70 (2015).
46. V. Maruthamuthu, M. L. Gardel, Protrusive activity guides changes in cell-cell tension during epithelial cell scattering. *Biophys. J.* **107**, 555–563 (2014).
47. B. D. Hoffman, A. S. Yap, Towards a dynamic understanding of cadherin-based mechanobiology. *Trends Cell Biol.* **25**, 803–814 (2015).
48. D. E. Leckband, J. de Rooij, Cadherin adhesion and mechanotransduction. *Annu. Rev. Cell Dev. Biol.* **30**, 291–315 (2014).
49. A. S. Yap, K. Duszyc, V. Viasnoff, Mechanosensing and mechanotransduction at cell-cell junctions. *Cold Spring Harb. Perspect. Biol.* **10**, a028761 (2018).
50. D. Pinheiro, Y. Bellache, Mechanical force-driven adherens junction remodeling and epithelial dynamics. *Dev. Cell* **47**, 391 (2018).
51. M. Westerfield, *The Zebrafish Book: A Guide for the Laboratory Use of Zebrafish (Danio Rerio)* (University of Oregon Press, 2007).
52. C. B. Kimmel, W. W. Ballard, S. R. Kimmel, B. Ullmann, T. F. Schilling, Stages of embryonic development of the zebrafish. *Dev. Dyn.* **203**, 253–310 (1995).
53. C. P. Choe *et al.*, Wnt-dependent epithelial transitions drive pharyngeal pouch formation. *Dev. Cell* **24**, 296–309 (2013).
54. Y.-S. Chu *et al.*, Force measurements in E-cadherin-mediated cell doublets reveal rapid adhesion strengthened by actin cytoskeleton remodeling through Rac and Cdc42. *J. Cell Biol.* **167**, 1183–1194 (2004).
55. Y. Arboleda-Estudillo *et al.*, Movement directionality in collective migration of germ layer progenitors. *Curr. Biol.* **20**, 161–169 (2010).
56. C. T. Rueden *et al.*, ImageJ2: ImageJ for the next generation of scientific image data. *BMC Bioinformatics* **18**, 529 (2017).
57. D. Banovic *et al.*, Drosophila neuroligin 1 promotes growth and postsynaptic differentiation at glutamatergic neuromuscular junctions. *Neuron* **66**, 724–738 (2010).
58. D. G. Lowe, Distinctive image features from scale-invariant keypoints. *Int. J. Comput. Vis.* **60**, 91–110 (2004).
59. X. Heiligenstein, P. Paul-Gilloteaux, M. Belle, G. Raposo, J. Salamero, eC-CLEM: Flexible multidimensional registration software for correlative microscopies with refined accuracy mapping. *Microsc. Microanal.* **23**, 360–361 (2017).